Metallography, Microstructure, and Analysis (2024) 13:114–129
https://doi.org/10.1007/s13632-023-01036-z

ORIGINAL RESEARCH ARTICLE

Prevalence of Heteroepitaxial Recrystallization in the Low Solvus High Refractory (LSHR) γ–γ′ Superalloy

Y. Lee[1] · E. Hershkovitz[1] · H. Kim[1] · K. N. Wertz[2] · E. J. Payton[3] · V. M. Miller[1]

Received: 3 August 2023 / Revised: 7 November 2023 / Accepted: 19 November 2023 / Published online: 23 January 2024

Abstract

Heteroepitaxial recrystallization (HeRX) is a recently discovered recrystallization mechanism that can occur during thermomechanical processing of Ni-base superalloys. It is important to understand this mechanism because it offers insights into grain size control, which is critical to the tensile, fatigue, and creep properties of superalloys. In this paper, HeRX activity in the low solvus high refractory (LSHR) is quantitatively characterized using combined energy-dispersive X-ray spectroscopy and electron backscatter diffraction. The formation of heteroepitaxially recrystallized grains is observed within the intermediate-misfit γ–γ′ superalloy LSHR; this suggests the HeRX is more widespread than initially thought. Microstructural imaging indicates that the presence of a coherent γ shell formed via inverse precipitation is not a necessary condition for the nucleation of HeRX grains. HeRX grains are found to comprise the large grain tail of the grain size distribution, regardless of processing condition. The extent of HeRX grain formation and growth in LSHR is determined as a function of strain, forging rate, and thermal history.

Keywords Ni-superalloys · recrystallization · HeRX

Introduction

Decades of advances in aeroengine turbine disk materials have consistently pushed the boundaries of engine capabilities [1]. For the current generation of powder metallurgical turbine disk alloys, fatigue life is largely governed by grain size distribution (GSD), thus control of the GSD during forging has been a subject of great interest in the manufacture and processing of superalloys for turbine disk applications. Typical processing schedules include sub-solvus forging followed by solution and aging heat treatments to control the evolution of the γ′ (strengthening phase) size distribution [2]. As the GSD evolves during the forging and solution-treating portions of turbine disk manufacturing, much of the research focus on the microstructural evolution of these components has been to understand the effects of recovery, recrystallization, and grain growth during these stages of processing. Previous investigations on the subject of plastic flow and microstructure evolution during forging have yielded important insights into the active mechanisms relevant to the development of the GSD, particularly the roles of superplasticity and discontinuous dynamic recrystallization (DDRX) [3–6].

One of the earliest efforts examining the effects of forging parameters on flow behavior and microstructural evolution in the superalloys was conducted by Immarigeon et al. [6]. Their work on alloy 713LC examined the effect of the grain size on flow behavior during sub-solvus forging and concluded that the size of the initial grains relative to the equilibrium size developed during forging determined whether steady-state flow or flow softening was observed. These behaviors were ascribed to superplastic flow and dynamic recrystallization, respectively. This initial work has been extended by numerous other authors through both modeling and experimental efforts such as the work of Koul et al. and Combres et al. [3, 7]. In addition to characterizing the effect of forging parameters on flow behavior, there has been significant work examining the active recrystallization mechanisms during forging [8, 9]. Such work conducted by

✉ Y. Lee
leey2@ufl.edu

[1] Department of Materials Science and Engineering, University of Florida, Gainesville, FL 32611, USA

[2] Air Force Research Laboratory, Wright-Patterson Air Force Base, Dayton, OH 45433, USA

[3] Department of Materials Science and Engineering, University of Cincinnati, Cincinnati, OH 45219, USA

Lindsley et al. demonstrated the effect of the initial γ and γ′ size on the active recrystallization mechanism during subsolvus forging, while Poelt et al. examined the evolution of the population of recrystallized grains during forging. In both cases, it was found that DDRX was the dominant mechanism responsible for grain refinement and recrystallization of the microstructure during forging.

Like many other microstructural transformations, recrystallization can either occur during the deformation process (dynamically) or subsequent to the deformation process (statically). In traditional thermomechanical processing of Ni-base superalloys, the reported recrystallization mechanisms are typically discontinuous and dynamic, with nucleation primarily occurring at preexisting high-angle boundaries [5, 10]. For the purposes of this manuscript, we will refer to this nucleation mechanism as “conventional DDRX”.

However, DDRX may also commence via other nucleation mechanisms. One of these is particle stimulated nucleation (PSN) of recrystallization [11–13]. In this mechanism, the mechanical mismatch between a hard second phase particle and the surrounding matrix promotes the accumulation of additional dislocations near the particle, resulting in a locally increased driving force for recrystallization. The preexisting particle-matrix interface is a low energy site for nucleation to occur; this combination makes hard second phase particles an effective nucleant for recrystallization. In case of Ni-base superalloys, incoherent primary γ′ particles can favor PSN [14, 15]. During thermomechanical processing, dislocations can accumulate preferentially in γ near primary γ′ to accommodate the mechanical mismatch.

A new recrystallization mechanism, heteroepitaxial recrystallization (HeRX), was first described in superalloys in 2016 by Charpagne et al. [16–18]. Because of the prior heat treatment, recrystallization was preceded by inverse precipitation in which a thin, coherent γ-like shell formed around the primary γ′ particles [19]. During deformation, dislocations will again preferentially accumulate near the γ′–γ core-shell structure either due to boundary pileups or increased backstresses from the hard core-shell structure. This pileup of dislocations provides the driving force for the growth of the γ shell during recrystallization. The end result of HeRX nucleation is a primary γ′ particle with a coherent γ shell. If the preexisting core–shell structure is thought of as a “particle”, HeRX could be considered a special case of PSN.

In the original work, on HeRX [16, 17], two preconditions for its occurrence were suggested. It was proposed that HeRX activity required a low interphase misfit between the γ and the γ′ phases, as well as the preexisting coherent γ shell on the particle resulting from inverse precipitation. However, recent theoretical work by Miller et al. suggests HeRX activity should be highly favorable over a wider range of alloys and forging conditions than previously thought [20].

Though many of the active processes during forging have been investigated in detail, there is still a gap that remains in our understanding of the interplay between these processes and the net effect on the GSD of a component. If HeRX is more widespread than originally thought, then it could play a significant role in microstructural evolution. The objectives of this work are to probe the range of experimental conditions over which HeRX is active and to explore the role of HeRX in overall microstructural evolution during deformation processing.

Experimental Procedures

Thermomechanical Processing

Low solvus high refractory (LSHR) is a polycrystalline Ni-based superalloy with an intermediate γ–γ′ misfit—measured at 0.23% at room temperature [21] and computationally predicted to increase at high temperature [22]. The actual composition is listed in Table 1 [23]. The as-received billet material was characterized in a previous investigation by Semiatin et al. and has a solvus temperature of 1157 °C [23]. Double-cone specimens were fabricated with an outer diameter of 63.2 mm and a total height of 31.6 mm using electro-discharge machining from billet material. From a 12 mm diameter base, the specimen tapered linearly to an outer rim of 2 mm height at the maximum diameter. The specimen geometry was mirrored across the horizontal plane that passed halfway through the 2 mm outer rim. This geometry was chosen to produce strain ranging between 0.1 and 1.0 between the outer rim and the center along the horizontal mirror plane, respectively, after forging to a 2:1 reduction.

Two of the four double-cone samples were subjected to a pre-deformation heat treatment to promote inverse precipitation such that the effect of inverse precipitation on HeRX activity within this alloy system could be assessed. For these heat treatments, specimens were placed into a furnace at 1093 °C, held for 2 hours at temperature, then cooled at 13 °C/min until the surface thermocouple reached 600 °C. After reaching 600 °C, they were allowed to air cool to room temperature. These heat treatments were selected based on the work by Charpagne et al. (5 °C/min cooling until 600 °C then air cooling) [16–18]; however, this work

Table 1 Nominal composition of LSHR in weight percent

Element	Co	Cr	Al	Ti	W	Mo	Ta	Nb	C	B	Zr	Ni
Weight %	20.4	12.3	3.5	3.5	4.2	2.7	1.6	1.5	0.045	0.027	0.05	Bal.

used a somewhat higher initial cooling rate. Despite this difference in the cooling rate, the heat treatment successfully induced inverse precipitation in the samples investigated (as addressed in Sect. “As-received material”).

All the specimens were isothermally forged at 1065 °C (92 °C below the γ′ solvus) with strain rates of 0.1/s and 0.001/s. The specimens were lubricated with boron nitride prior to placement in the press to minimize the effect of friction between the die and the specimen during forging. Specimens were placed into the forging press at room temperature and heated to the forging temperature as quickly as possible (17 °C/min) before forging commenced. The specimens were held for 5 mins at the forging temperature before forging, and then water quenched within 3 s of completion of forging to freeze in the microstructure at the forging temperature and suppress γ′ precipitation.

A schematic of the strain and strain rate gradients produced in the samples is shown in Fig. 1, as calculated using the DEFORM software (Scientific Forming Technology Corporation). Heat transfer was considered in the calculation using the temperature-dependent flow stress model from Semiatin et al. [4]. DEFORM-predicted stress-strain curves for each of the five sites described in Fig. 1 are shown for reference in Fig. 2.

The combination of deformation conditions and thermal histories used to generate the samples used in this investigation yielded four total specimen conditions, designated 0.1/s, 0.1/s HT, 0.001/s, and 0.001/s HT, where the designations correspond to initial strain rate and whether the specimen underwent the pre-deformation heat treatment.

Microstructural Characterization

The as-deformed specimens were quartered using wire electrical discharge machining (EDM), producing sections as illustrated in Fig. 1. A polished surface suitable for electron backscattered diffraction (EBSD) was obtained by grinding with successively finer silicon carbide abrasive paper, followed by polishing using a 1 μm alumina suspension and finally vibratory polishing with a 0.05 μm colloidal silica suspension. Microstructural characterization was accomplished using a coupled energy-dispersive spectroscopy (EDS)—EBSD technique conducted in an FEI Verios 460L scanning electron microscope (SEM) at

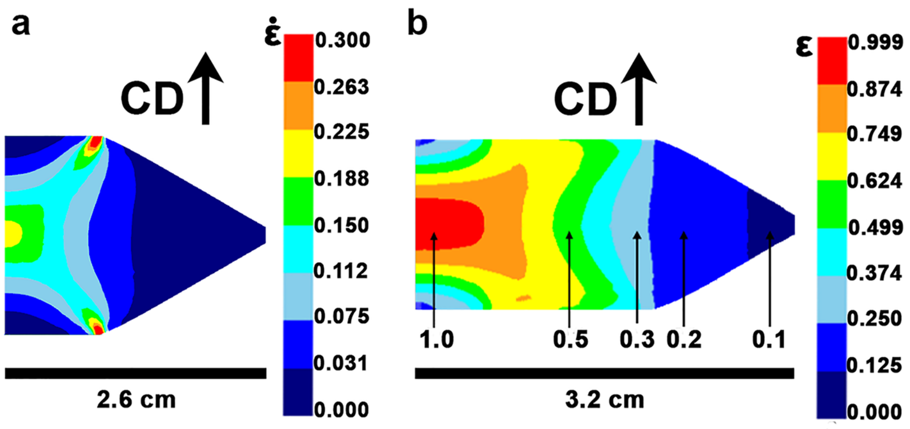

Fig. 1 Schematic of the strain rate (**a**) and strain (**b**) gradients present after 2:1 reduction in the double-cone specimens characterized in this work. The location of microstructural analyses relative to deformed outer diameter (in mm) are indicated with arrows. These locations were assigned numeric labels sequentially from 1-5 starting from the outer diameter

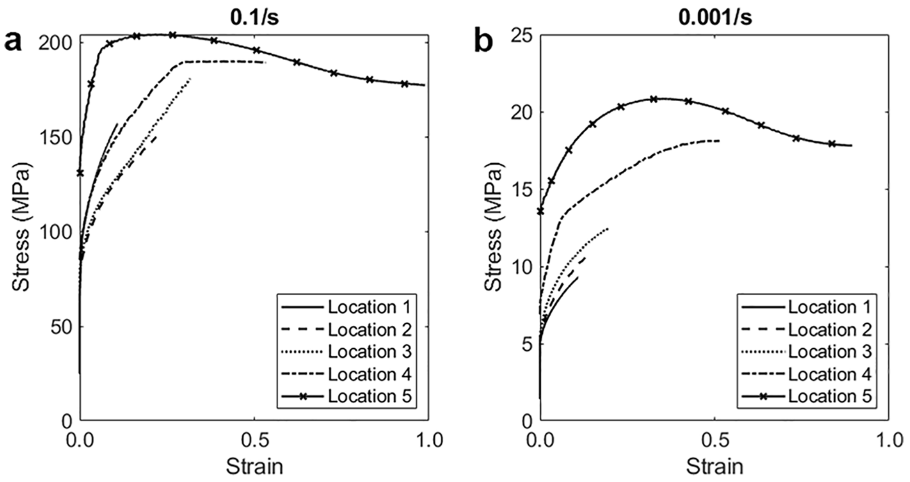

Fig. 2 DEFORM-calculated stress-strain curves the five locations on the double cone specimens at each of the two applied compression rates, corresponding to initial strain rates of 0.1/s (**a**) and 0.001/s (**b**)

15 kV operating voltage and 13nA beam current with a step size of 0.25 µm. As the γ and γ′ have the same crystal point group m$\bar{3}$m, EBSD alone is insufficient to discriminate between the matrix and the second phase.

However, recent work using combined EDS-EBSD allowed for the discrimination between the primary γ′ and the surrounding γ matrix in the EBSD scans using chemically assisted imaging with built-in spectrum matching [18]. A similar approach was used for the microstructural characterization in this work.

Characterization of atomic structure and elemental distribution were carried out using scanning transmission electron microscopy (STEM) and energy-dispersive X-ray spectroscopy (EDS). Cross-sectional specimens for STEM and EDS studies were prepared by first using a FEI Helios G4 PFIB CXE Dual Beam FIB/SEM equipped with an EDAX Velocity EBSD CMOS camera to map regions of interest on the bulk sample. Once the lamella was lifted out and mounted on a copper grid with the PFIB, the sample was thinned using a FEI Helios Dualbeam Nanolab 600 FIB. A final cleaning cycle of the cross-sectional specimens was conducted using Ga ions at 2 kV. High-angle annular dark-field (HAADF) imaging in STEM was performed using a Themis Z (Thermo Fisher Scientific) equipped with a probe aberration corrector and a four-quadrant Super-X EDS detector. The accelerating voltage of the microscope was 200 keV and the semi-convergence angle was 22 mrad. EDS elemental maps were obtained with a 100 pA beam current and a pixel dwell time of 20 µs.

In the present work, just under 20% area fraction of primary γ′ was detected in the as-deformed states (described later), as compared to an equilibrium γ′ area fraction of approximately 32% predicted by Thermo-Calc [24] under the deformation conditions. While this is a substantial discrepancy, EDS is only able to detect the largest primary γ′ particles due to interaction volume limitations of EDS under these imaging conditions. Small primary γ′ and any secondary or tertiary γ′ will not be detected, resulting in an artificially low γ′ phase fraction. As these smaller γ′ are unlikely to substantially participate in HeRX or be present at the forging temperature, this discrepancy is not anticipated to substantially affect the present results.

The open-source MATLAB package MTEX [25] was used for EBSD data post-processing. EBSD data sets were collected at the regions labeled in Fig. 1 and were processed to identify and characterize the HeRX grains within the microstructure. Grain boundaries were calculated using a 5° threshold misorientation angle. Additionally, the Σ3 annealing twins within the microstructure were identified and merged into their parent grains, in order that they be counted and considered as internal crystal defects rather than distinct grain boundaries.

As part of the distinct phenomenology of HeRX is the presence of a coherent $\gamma-\gamma'$ boundary, grains containing such a boundary were identified as potential HeRX grains. The threshold misorientation angle for a coherent primary $\gamma'-\gamma$ boundary was set at 3°. The 3° threshold was selected to ensure that grains where perfect coherency was disrupted by continued deformation were still counted as HeRX. The analysis was also conducted with a 1° threshold; the conclusions are robust to choice of threshold within this range. Additionally, grain orientation spread (GOS) values were used to assess the accumulated internal misorientation within a grain; low-GOS values suggest a given grain has undergone recrystallization and has not accumulated much additional strain. In this manuscript, a GOS threshold of 1° is used for microstructural segmentation. An example dataset highlighting the segmented microstructure is illustrated in Fig. 3. These microstructure fractions can also be presented as a stacked bar chart to represent the breakdown of the microstructure at a particular location. To characterize the behavior of the HeRX grains within this material, the area fraction of γ containing a coherent primary γ′, the fraction of coherent $\gamma-\gamma'$ boundary, and the size of the potential HeRX γ grains are each quantified at all of the marked locations marked in Fig. 1. The equations used for the quantitative description of the microstructure are given in Eq. 1, 2 and 3.

The coherent boundary fraction (CBF) is calculated according to Eq. 1, where $\sum_1^n \mathrm{CB}_n^{\gamma-\gamma'}$ is the sum of all coherent γ–γ′ boundary segment lengths detected in the scan over the sum of all γ–γ′ boundary segment lengths in the scan, $\sum_1^k \mathrm{B}_k^{\gamma-\gamma'}$.

$$f_{\mathrm{coherent}} = \frac{\sum_1^n \mathrm{CB}_n^{\gamma-\gamma'}}{\sum_1^k \mathrm{B}_k^{\gamma-\gamma'}} \tag{1}$$

The average HeRX shell thickness (R_{average}) is given by Eq. 2 where $r_{\mathrm{eq}}^{\mathrm{HeRX}\gamma}$ and $r_{\mathrm{eq}}^{\mathrm{HeRX}\gamma'}$ are the average HeRX γ and

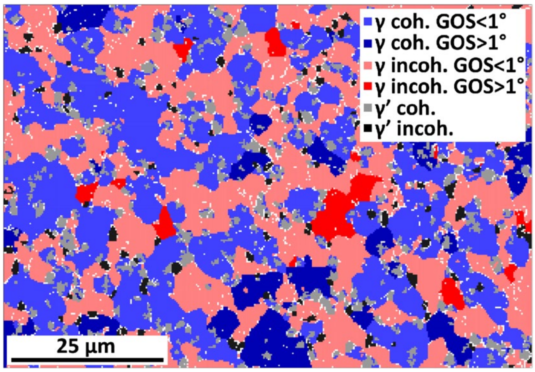

Fig. 3 Example dataset from the $\epsilon = 0.1$ region of the fast forged, un-heat-treated sample. The microstructure is segmented by phase, grain orientation spread (GOS), and the presence of a coherent $\gamma-\gamma'$ boundary. Grains presented in light or dark blue are suspected HeRX grains, as they contain coherent $\gamma-\gamma'$ boundaries

HeRX γ′ circle-equivalent radii at each strain level along the gradient, described explicitly below.

$$R_{\text{average}} = r_{\text{eq}}^{\text{HeRX}\gamma} - r_{\text{eq}}^{\text{HeRX}\gamma'} \tag{2}$$

Equation 3 shows how the equivalent radii are calculated, where A_{HeRX}^{γ} and $A_{\text{HeRX}}^{\gamma'}$ are the average areas of the HeRX γ and γ′ at each strain level, obtained directly from EBSD dataset. Note that by definition the HeRX γ′ is located within its γ grain, increasing the γ grain radius, so the area of the particle is included in the calculation of the equivalent radius.

$$r_{\text{eq}}^{\text{HeRX}\gamma} = \sqrt{\frac{A_{\text{HeRX}}^{\gamma} + A_{\text{HeRX}}^{\gamma'}}{\pi}}, r_{\text{eq}}^{\text{HeRX}\gamma'} = \sqrt{\frac{A_{\text{HeRX}}^{\gamma'}}{\pi}} \tag{3}$$

To evaluate the uncertainty present in the measurement of HeRX behavior due to microstructural variability, multiple additional EBSD scans were taken in the largest area of constant strain in the 0.1/s HT specimen. The standard deviation in the metrics used to describe HeRX activity are presented in Table 2, and the data are also included throughout the presentation of results. Approximately 20300 µm^2, corresponding to over 7000 grains, were used to analyze the impact of microstructural variability on measurement uncertainty. It is expected that error on the same order of magnitude seen in this region is reasonable for each data point.

Table 2 Mean and standard deviation of all metrics used to quantify HeRX activity. The results here were obtained from the largest region of constant strain in the fast-forged heat-treated sample

Metric	CBF	Mean HeRX γ diameter (µm)	Fraction of HeRX γ
Mean	0.71	2.84	0.66
σ	0.09	0.08	0.03

Thermodynamic Simulations

The CALPHAD software Thermo-Calc [24] is used to predict composition variation in the γ and γ′ phases as a function of temperature for the nominal composition provided in Table 1, similar to the work done by Charpagne et al. [16]. This information was used to assess the efficacy of the pre-deformation heat treatments used to induce inverse precipitation.

Results

As-Received Material

Characterization of the as-received (AR) and as-heat-treated (AHT) microstructures was accomplished using the EDS-EBSD technique described in Sect. "Microstructural characterization". Backscattered electron (BSE) micrographs were also acquired. Representative micrographs and IPF maps of each initial condition are shown in Fig. 4. EDS-EBSD scans of the AR and AHT material revealed the presence of γ grains containing coherent primary γ′ in the microstructure of both specimens. However, the pre-deformation heat-treatment increased the coherent boundary fraction from approximately 20% in the AR condition to 44%, as

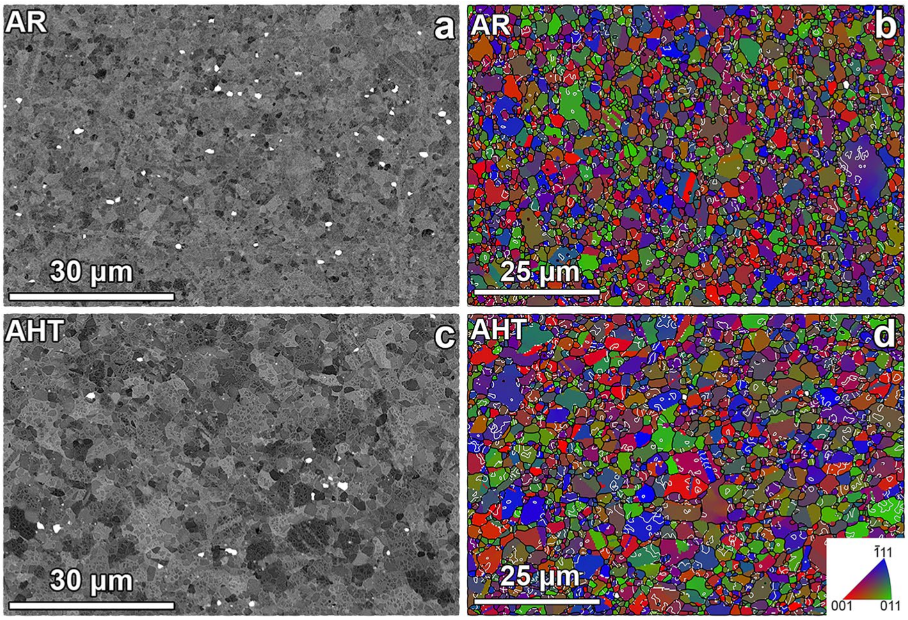

Fig. 4 Representative IPF (**b**, **d**) maps and BSE (**a**, **c**) images from specimens in the as-received (AR) (**a**, **b**) and the as-heat-treated (AHT) (**c**, **d**) conditions. In the IPF maps, the coherent γ–γ′ boundaries are displayed in white, with all other boundaries in black

Table 3 Coherent boundary fraction for the as-received and as-heat-treated specimens

	As-received	As-heat-treated
Coherent boundary fraction	0.20 ± 0.01	0.44 ± 0.04

shown in Table 3. Fig. 5 also illustrates a substantial increase in the area fraction of coherent γ grains. The observed increase in the CBF is most likely a consequence of inverse precipitation.

As-Soaked Microstructures

To ascertain the microstructures of the specimens immediately prior to deformation, specimens were prepared in an "as-soaked" condition. As the isothermal forging of the specimens was conducted after 5 minutes of temperature saturation, the potential effect of such heating profile on the microstructure evolution was investigated. Specimens in the AR and AHT conditions were heated to the deformation temperature (1065 °C), held for 5 minutes, and immediately quenched; the process will be referred to as a *soak*. IPF maps of the as-soaked microstructures, representing the structure at the moment deformation begins, are shown in Fig. 6 and the area fraction breakdown of the microstructure is illustrated in Fig. 5. In the AR samples, the soak decreases the fraction of high-GOS grains but has little influence on the fraction of coherent gamma. Conversely, in the AHT samples the soak substantially decreases the microstructural fraction of coherent gamma, increasing the amount of incoherent gamma. This is consistent with the instability of the inverse precipitation core-shell structures at high temperature [16]. At the conclusion of the soak the AHT specimens still have approximately 30% of the microstructure composed of coherent γ grains, in comparison to only approximately 20% for the AR specimens. Neither heat treatment condition experiences significant dissolution of the primary γ′ during the soak.

Microstructure of the As-Deformed Specimens

As the presence of a coherent primary γ′ boundary is indicative of (but not necessarily exclusive to) an HeRX

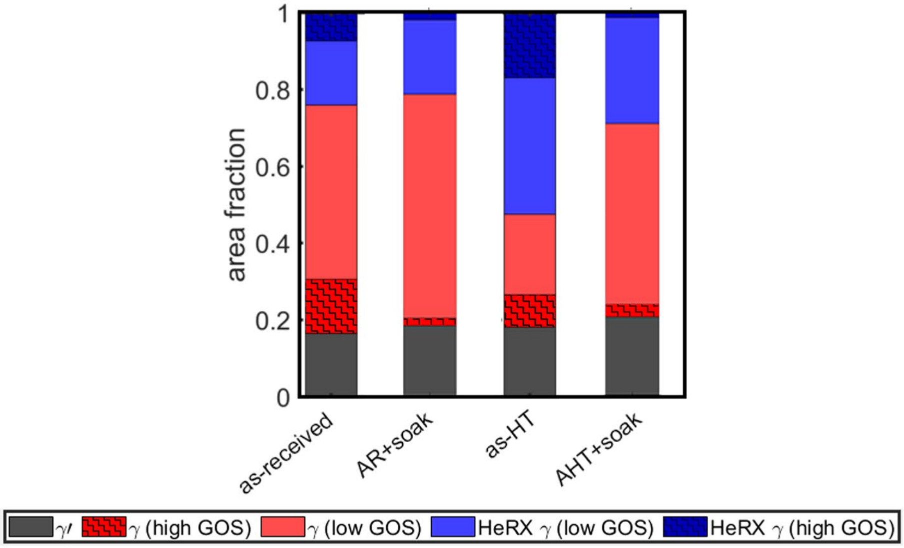

Fig. 5 Microstructure fractions present in the AR, AHT, and as-soaked microstructures. The soak process in as-received samples does not change the fraction of coherent γ while the overall stored energy of the system decreases. Notably, a substantial decrease in the fraction of coherent γ is observed from as-heat-treated samples due to the instability of the coherent γ shell at the elevated temperature

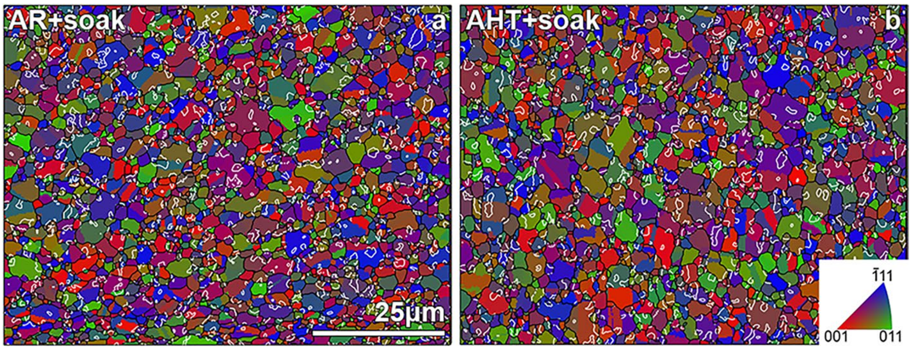

Fig. 6 Representative IPF maps of the AR + soak (**a**) and AHT + soak (**b**) microstructures

grain, the γ grains containing coherent boundaries identified using EDS-EBSD were taken to be *potential* HeRX γ within the microstructure. Example data sets from all samples in the lowest (ϵ = 0.1) and highest (ϵ = 1.0) strain regions are shown in Figs. 7 and 8, respectively; the coherent boundary segments are shown in white. Potential HeRX grains were observed to form frequently within the microstructure at all strains across the specimen radius for all specimens characterized, even in the specimens that did not receive the pre-deformation heat treatment. The morphology of HeRX grains in the LSHR superalloy is often "lobed" rather than the previously observed core-shell structure (Fig. 9). Quantification of the potential HeRX features will be addressed in the subsequent sections.

In some high-strain regions of the microstructure near-coherent C-type and near-twin-oriented T-type precipitates were observed [26, 27]. A clear example of T-type precipitates is the large blue grain in the upper left of Fig. 8c.

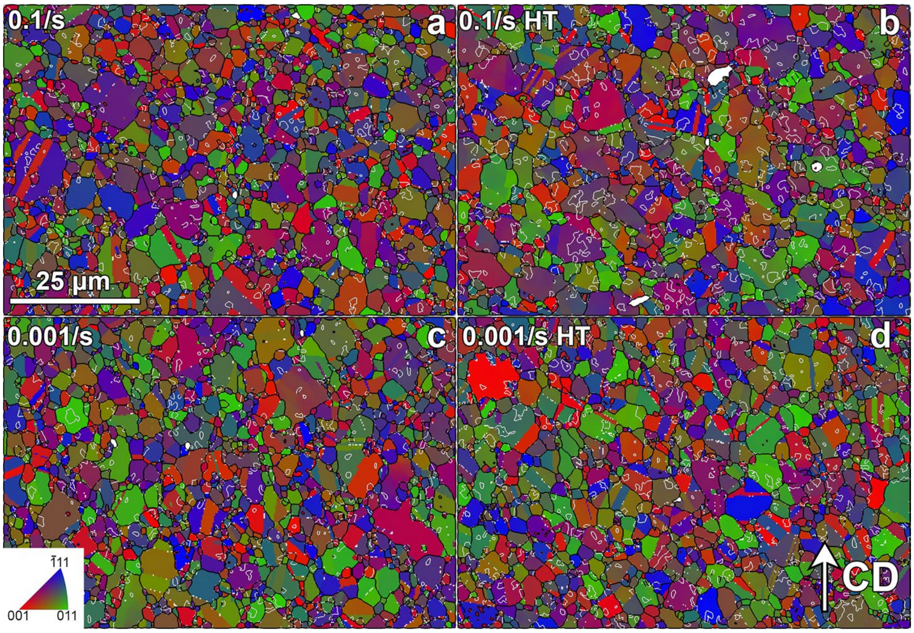

Fig. 7 Microstructures of all samples (ϵ = 0.1). Coherent γ–γ′ boundaries are displayed in white, with all other boundaries displayed in black. The arrow indicates the compression direction. Each deformation rate and preheat treatment condition combination is shown: **a** 0.1/s no preheat-treatment, **b** 0.1/s preheat-treated, **c** 0.001/s no preheat-treatment, and **d** 0.001/s preheat-treated

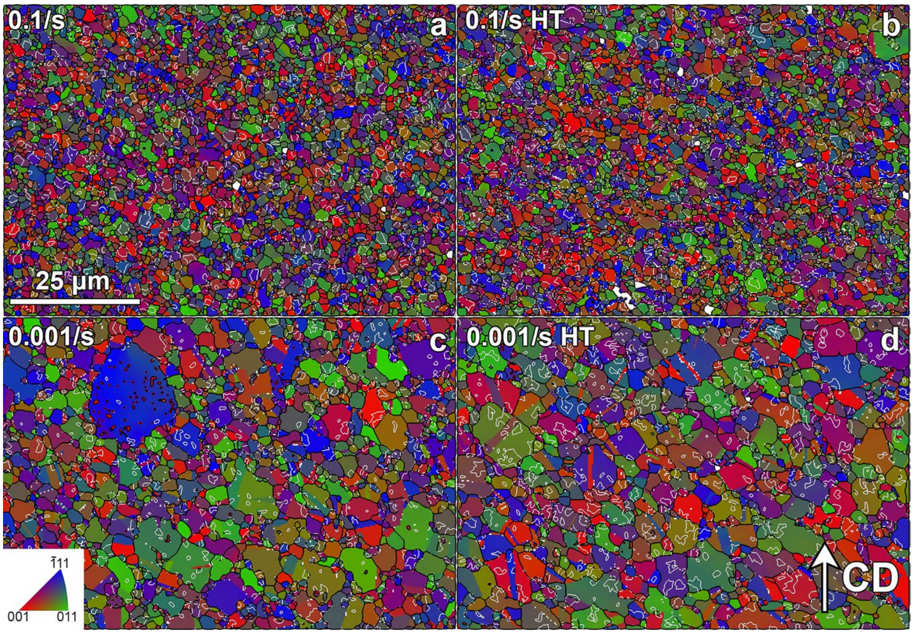

Fig. 8 Microstructures of all samples (ϵ = 1.0). Coherent γ–γ′ boundaries are displayed in white, with all other grain boundaries displayed in black. The arrow indicates the compression direction. Each deformation rate and preheat treatment condition combination is shown: **a** 0.1/s no preheat treatment, **b** 0.1/s preheat-treated, **c** 0.001/s no preheat-treatment, and **d** 0.001/s preheat-treated

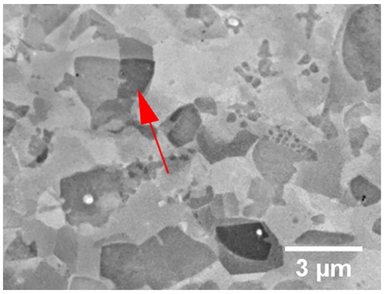

Fig. 9 HeRX grains in LSHR often have a lobed morphology rather than a core-shell structure. No evidence of a preexisting shell formed by inverse precipitation is observed

Area Fraction of Potential HeRX γ

The area fraction of γ grains containing a coherent primary γ' was calculated along the strain gradient for each sample characterized, and is shown for all samples in Fig. 10. Exposure to the pre-deformation heat treatment enhances the overall area fraction of potential HeRX γ within the microstructure. Additionally, the prevalence of potential HeRX within the microstructure decreases sharply in the fast-forged samples, indicating an apparent threshold strain where the HeRX grains are consumed by other dynamically recrystallized grains. This interpretation is further supported in Sect. "Microstructural segmentation" below.

Coherent Boundary Fraction

In an effort to further describe the prevalence of HeRX activity within the microstructure and its sensitivity to forging parameters, the fraction of coherent γ–γ' boundary segments was calculated along the strain gradient for each sample (shown in Fig. 10). Similarly to the area fraction of HeRX γ, samples exposed to a pre-deformation heat treatment displayed higher overall coherent boundary fractions at low strains, an expected consequence of inverse precipitation. The slow-forged specimens generally maintained these coherent boundary fractions to high strains, while the fast-forged specimens underwent a small drop in coherent boundary fraction. The drop in coherent boundary fraction is much smaller than the drop in area fraction of suspected HeRX grains (indicated by coherent boundary fraction), suggesting that the HeRX grains are only partially consumed by the advancing conventional DDRX front. This is further supported by the reduction in calculated shell thickness.

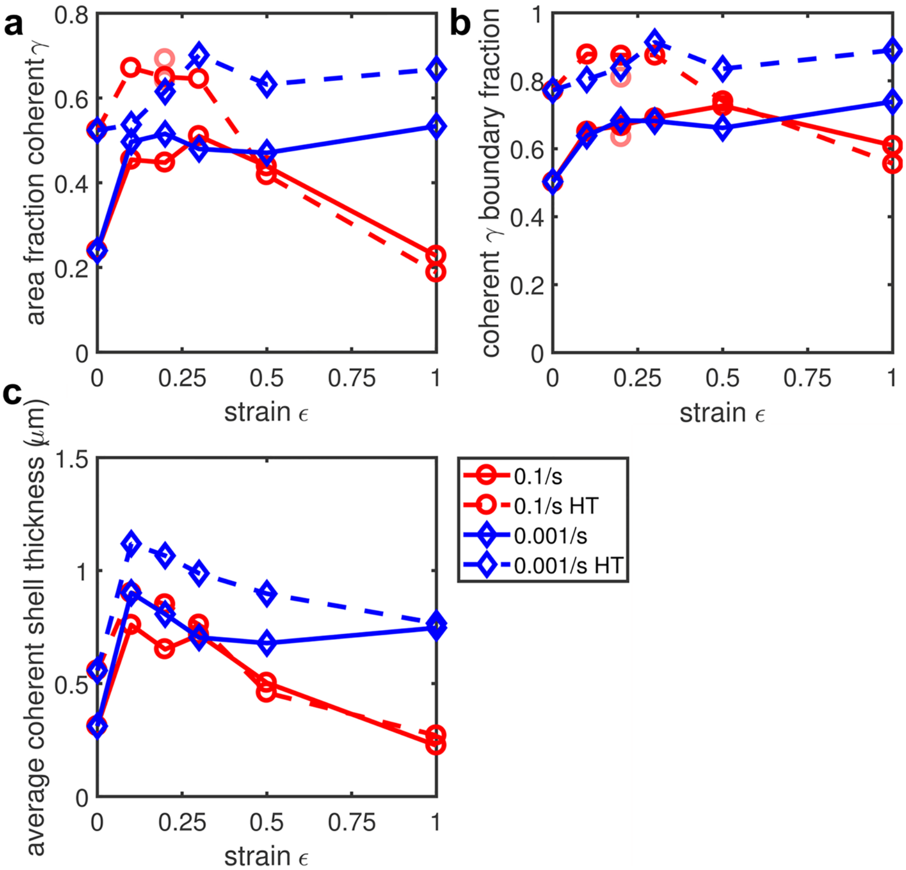

Fig. 10 Metrics of potential HeRX activity as a function of strain for each thermomechanical condition. **a** Area fraction of coherent γ as a function of strain. **b** Fraction of coherent γ-γ' boundaries as a function of strain. **c** Average coherent shell thickness for each HeRX grain as a function of strain

Average HeRX Shell Thickness

To describe the variation in potential HeRX γ size relative to that of the γ′ nuclei across forging conditions, the average shell thickness ($R_{average}$) was calculated along the strain gradient for each sample. This metric is particularly important, because an increase in shell thickness with strain can be used to distinguish HeRX activity from inverse precipitation. In the fast-forged samples, the average shell thickness is observed to decrease from a maximum of ~1 µm to a size on the order of that of the γ′ (Fig. 10). In contrast, the average shell thickness of the slow-forged samples remains consistently larger than γ′ along the entire strain gradient, converging to a value ~4 times the size of the γ′ in the highest strain region. Notably, the average shell thickness in the slow-forged samples is larger than those observed in the fast-forged samples.

As with the other metrics of HeRX activity, the pre-deformation heat treatment was confirmed to increase the overall average shell thickness. However, there is some deviation from this trend in the fast-forged samples at both $\epsilon = 0.3$ and $\epsilon = 0.5$; this may be due to slight differences in average HeRX γ′ size between the AR and AHT fast-forged samples.

Microstructural Segmentation

To distinguish HeRX activity in the deformed specimens, the indexed microstructure was segmented into five bins based on phase, GOS, and boundary coherency (Fig. 11). The first bin consists of primary γ′; these particles did not evolve much during processing, as evidenced by the approximately constant phase fractions across all processing conditions. The remaining four bins divide the γ phase grains based on GOS (as a proxy for recrystallized versus unrecrystallized) and the presence of a coherent boundary with a γ′ particle (as a proxy for HeRX versus not HeRX). Grains with low GOS (< 1°) values have little internal misorientation, indicating that they were either "hard" during deformation, and as such did not undergo substantial strain, or that they have recrystallized. Grains with high-GOS values have a high density of geometrically necessary dislocations and likely remain in the as-deformed (unrecrystallized) state or accumulated significant strain after recrystallization occurred [28]. Using these five bins (γ′, low-GOS γ, high-GOS γ, low-GOS HeRX, and high-GOS HeRX), each grain is classified to assess the fraction of unrecrystallized (UnRX), DDRX grains, and the relative prevalence of HeRX as a function of strain and pre-deformation heat treatment (Fig. 11).

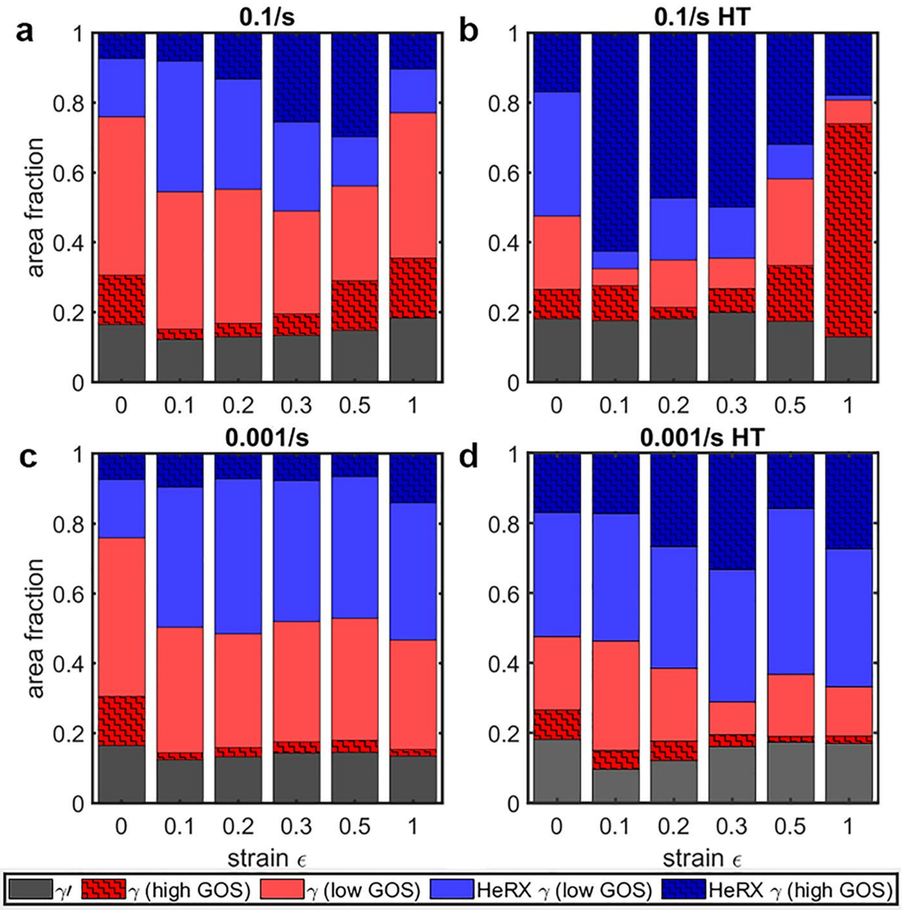

Fig. 11 Breakdown of the microstructure of each sample along the strain gradient. The relative area fraction of coherent HeRX γ (high + low GOS) within the microstructure is generally enhanced by the pre-deformation heat treatment to encourage inverse precipitation. Grains that have a high GOS have high internal misorientation, indicating a high geometrically necessary dislocation density and suggesting that they are in the as-deformed state. Grains with low GOS values are likely undeformed or as-recrystallized. Shades of blue indicated likely HeRX γ grains, as identified by their internal coherent γ–γ′ boundary. Shades of red indicate all other γ grains. Primary γ′ are shown in dark gray. Each plot shows a different combination of deformation rate and preheat treatment condition: **a** 0.1/s no preheat-treatment, **b** 0.1/s preheat-treated, **c** 0.001/s no preheat-treatment, and **d** 0.001/s preheat treated

The fraction of HeRX grains increases most substantially within the first 0.1 of strain—consistent with previous observations that HeRX occurs at lower strains than most other DRX mechanisms. After the first 0.1 strain, the fraction of HeRX grains is relatively stable with further strain in the slow-forged specimens, though the AHT slow-forged specimens do show a slight increase in overall area fraction with increasing strain, particularly for potential HeRX grains with high GOS.

For the fast-forged specimens, the difference in observed behavior between the AR and AHT specimens is striking. In the absence of the pre-deformation heat treatment, the area fraction of suspected HeRX grains increases with increasing strain up to 0.3, with increasing fractions of the likely HeRX grains having high GOS. Above 0.3 strain, the overall fraction of likely HeRX grains decreases with increasing strain; they are primarily replaced by an increasing fraction of low-GOS grains without a coherent boundary (most likely other DDRX grains formed via conventional mechanisms).

In the fast-forged specimens that received the pre-deformation heat treatment, the fraction of grains with a coherent boundary is much higher even at zero strain, suggesting the occurrence of inverse precipitation. After small strains, these coherent γ have accumulated internal misorientation. With moderate strain, it appears that additional HeRX occurred, resulting in a greater fraction of low-GOS coherent γ up to again 0.3 strain. At higher strains, the fraction of likely HeRX grains decreases in favor of γ without a coherent boundary. Interestingly, the non-HeRX microstructure segments overall retained substantially more internal misorientation than in the fast-forged samples without a preliminary heat treatment.

Grain size comparison of the HeRX and matrix γ

As one of the objectives of the current work was to assess the impact of HeRX on the as-deformed GSD, it was of interest to compare size distributions of coherent γ grains to the overall γ population. Fig. 12 displays the box plots of both the coherent (potential HeRX) and non-coherent matrix γ grains for each strain. When comparing the size of the coherent γ to the matrix γ grain size across all samples, it was found that the median HeRX and matrix γ grains are nominally the same size at almost every strain level. However, in the AHT samples the largest coherent γ are much larger than the largest matrix γ grains.

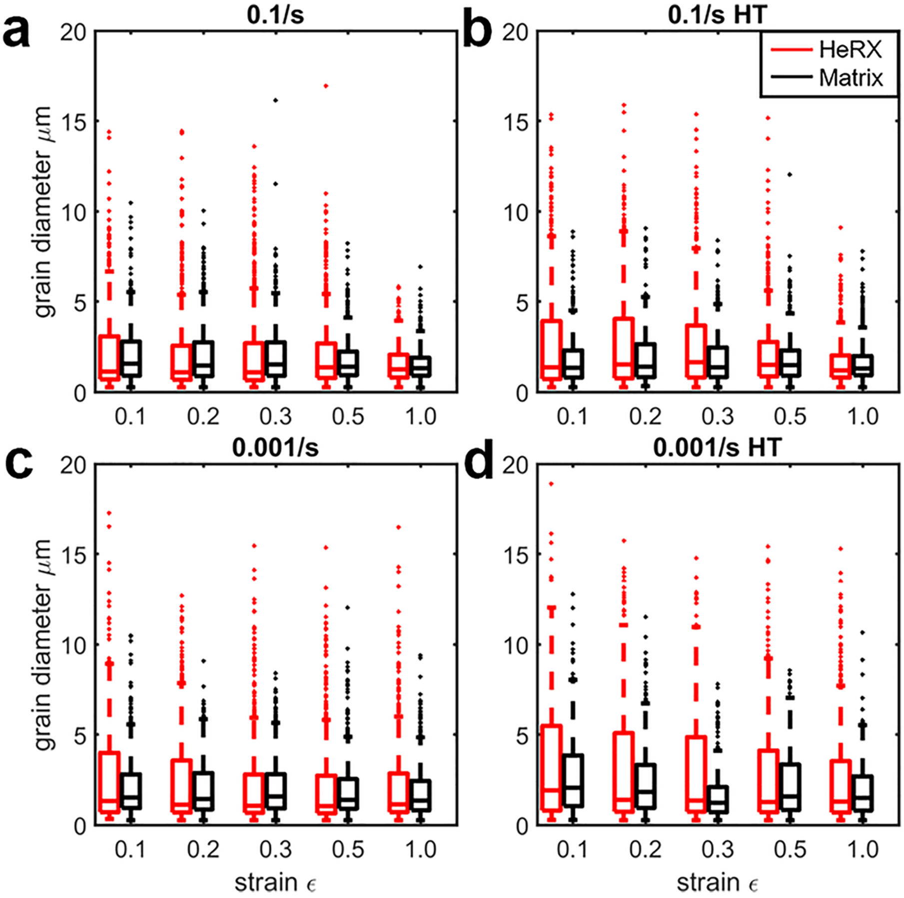

Fig. 12 Comparison of the HeRX γ and matrix (non-HeRX) γ grain sizes. Each deformation rate and preheat treatment condition combination is shown: **a** 0.1/s no preheat-treatment, **b** 0.1/s preheat-treated, **c** 0.001/s no preheat-treatment, and **d** 0.001/s preheat-treated. As is shown above, in the heat-treated specimens the largest potential HeRX grains are generally larger than the largest matrix γ

TEM Analysis of Potential HeRX Grains

TEM analysis was conducted on foils extracted from the 0.1/s HT specimen. The purpose of the TEM analysis was to investigate the extent of coherency of the identified potential HeRX grains and to look for evidence of inverse precipitation. This specimen was selected because it was both heat treated to promote inverse precipitation and spent less time at the forging temperature due to the higher loading rate. Any inverse precipitation that occurred has the greatest likelihood of remaining present in this specimen.

Figure 13 shows three HAADF-STEM images along a [112] zone axis of a suspected HeRX grain containing two primary γ′ particles. As shown, there are dislocations which loop around the particles at the interface. At the nanoscale, strong lattice alignment is observed across the γ–γ′ interface. Both γ′ particles are largely coherent, likely with some misfit dislocations.

STEM EDS is used to assess the chemistry near the interface, as shown via a line scan in Fig. 14 and maps in Fig. 15. As shown, the γ region is filled with tertiary γ′ precipitates with a clear particle denuded zone near the interface with the primary γ′ particle. The EDS data show a clear distinction

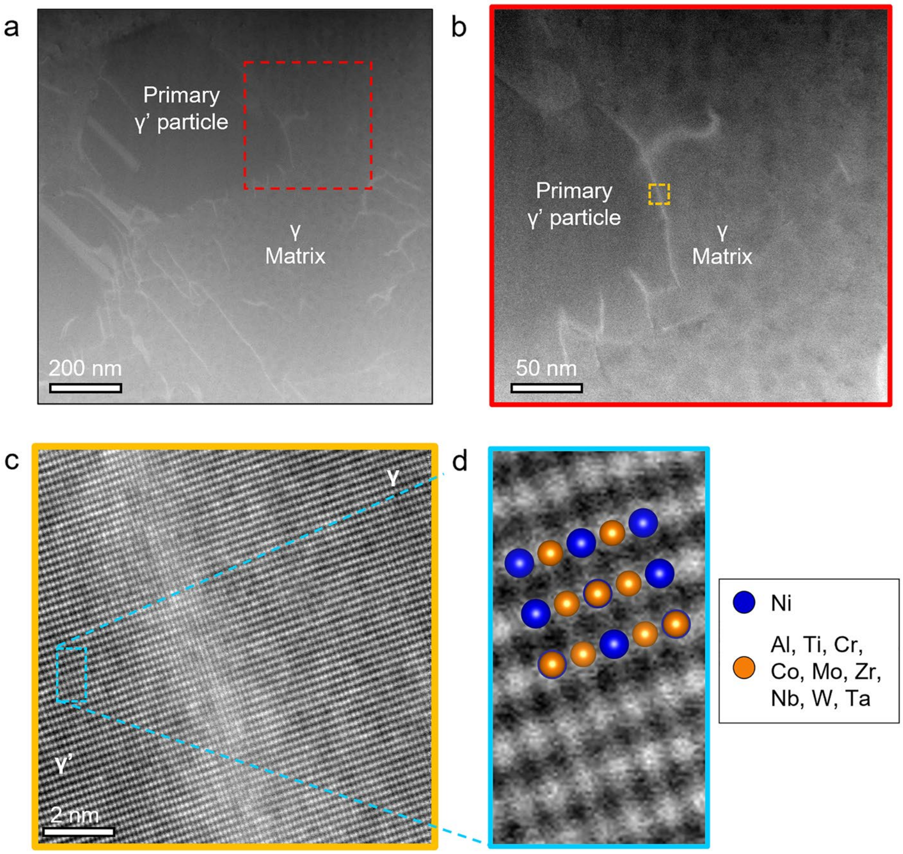

Fig. 13 HAADF-STEM images of the LHSR alloy. **a** Low magnification image showing multiple primary γ′ particles. **b** Magnified image of the red dashed box in (**a**) that shows round, darker areas on the right side of the image, indicative of tertiary γ′ precipitates. **c** Magnified image of the dashed orange box in (**b**) highlighting the coherent γ-γ′ interface. **d** High magnification HAADF-STEM image along the [112] zone axis from (**c**) marked by the blue dashed box, showing the atomic structure of the $L1_2$ γ′ LHSR alloy

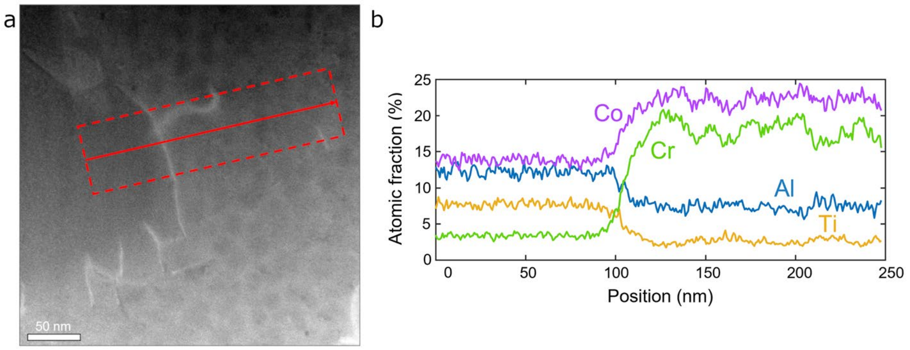

Fig. 14 EDS line scan across the γ–γ′ interface. **a** HAADF-STEM image of the region of interest where EDS was conducted. The line scan location is denoted by the red arrow in the dashed red box. **b** Results from the EDS line scan across the γ–γ′ interface. The composition gradients on the γ side of the interface suggest the remnant of inverse precipitation

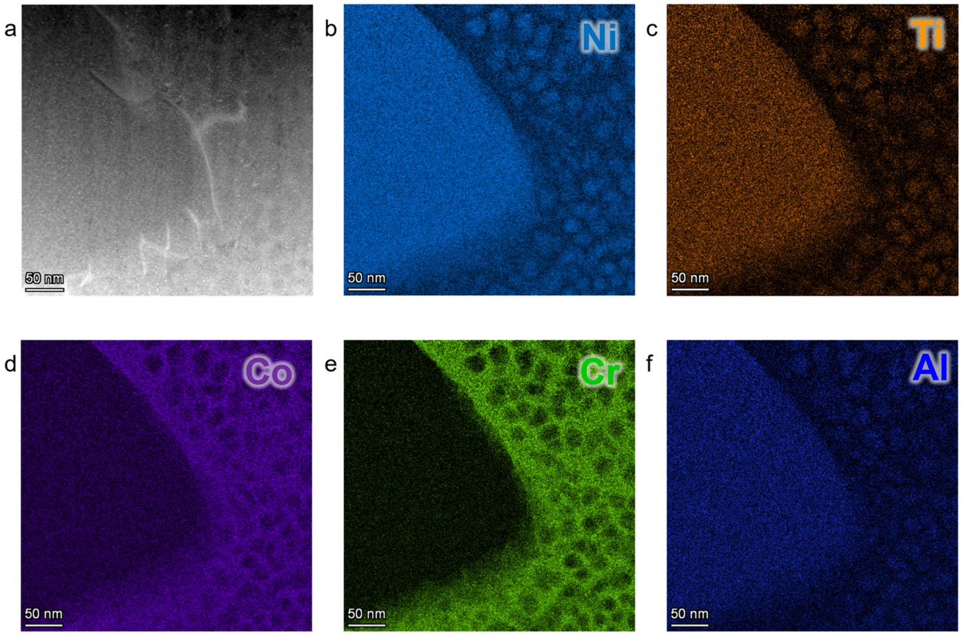

Fig. 15 **a** HAADF-STEM image across a likely HeRX γ–γ′ interface. **b**–**f** individual EDS maps on (**a**) Ni, Ti, Co, Cr, and Al

between the γ and the γ′ chemistry, but there is a gradient in chemistry on the γ side of the interface, particularly for Co and Cr. This approximately 20 nm thick region of gradient chemistry suggests the remnant of an inverse precipitation shell.

Discussion

The interplay between the HeRX recrystallization mechanism and conventional DDRX mechanisms in Ni superalloy is critical to understanding the grain size evolution during thermomechanical processing. HeRX is unique because it avoids the recovery-limited nucleation challenges of conventional recrystallization by allowing the preexisting primary γ′ particle to serve as a recrystallization nucleus. This effectively avoids any curvature-related energy penalties associated with conventional nucleation and allows recrystallization to initiate at very low dislocation densities [20]. HeRX does have limitations. First, the total number of potential nucleation sites has an upper bound set by the number of primary γ′ particles in the microstructure. Second, by initiating nucleation at very low dislocation densities, the growth of HeRX grains sometimes stagnates due to a lack of further driving force (i.e., differences in local dislocation densities) before the full volume of material is consumed, resulting in “island” grains.

Similarly, there are substantial experimental challenges associated with the characterization of HeRX grains. First among these is the stereological challenge associated with the detection of HeRX grains. As HeRX grain detection relied on the direct observation of the coherent γ–γ′ interface, an HeRX grain will not be detected if the 2D section plane does not intersect a substantial amount of both phases. As such, it is not trivial to convert from the area fractions reported here to bulk volume fractions.

Additionally, the double cone methodology used in nearly every study of HeRX to date makes it impossible to quantitatively decouple the magnitude of strain, strain rate, and local stress (cf. Fig. 2). While this is fine for qualitative comparison, it results in limited ability to appropriately evaluate the balance between dislocation accumulation and dynamic recovery. Future work using right circular cylinders or similar specimen geometry is recommended to deconvolve these effects.

Despite these complications, there are several relatively clear points emerging from this study, discussed below.

The Role of Inverse Precipitation

Half of the specimens used in this work were subjected to a preliminary heat treatment intended to induce inverse precipitation. This heat treatment was designed based on the prior work of Charpagne et al. [16–18] and Katnagallu et al. [19]; however, the cooling rate used in the present work is slightly higher. Despite this difference, there is substantial evidence that inverse precipitation did occur. This is supported by the substantial increase in coherent boundary fraction after heat treatment (Table 3) and the increase in microstructure fraction of coherent γ grains. Evidence of the remaining “γ-like” shell was observed via TEM EDS. As noted in the previous work by Charpagne et al., the core-shell inverse precipitation structures are unstable and begin to dissolve upon exposure to high temperatures, as illustrated in the as-soaked microstructures.

The reason for inverse precipitation can be explained using Thermo-Calc simulations for LSHR are shown in Fig. 16. For verification of the simulation, the calculated γ′ solvus of 1132 °C was compared to the experimental measurement of 1157 °C [23] and found to be in relatively good agreement. Similarly to Charpagne et al., an increase in the concentration of γ-partitioning elements in the γ′ at elevated temperature is predicted, such that inverse precipitation of γ phase at the rim of the primary γ′ is possible [16, 17]. This indicates that inverse precipitation is predicted to occur in the samples exposed to pre-deformation heat treatment, thereby generating an initial coherent γ shell around the primary γ′ in the AHT samples prior to compression.

From the comparison of the deformed microstructures between the heat-treated samples and those without pre-deformation heat treatment compressed at the same rate, it is readily apparent that the heat treatment enhances HeRX activity within the microstructure. In Figs. 10 and 11, the overall area fraction of potential HeRX γ is observed to be greater in the heat-treated samples. The increase in potential HeRX activity is also supported by the overall higher fraction of coherent γ–γ′ boundary (see Fig. 10) in these samples.

Additionally, a greater fraction of coherent boundary is an expected consequence of inverse precipitation, suggesting that the initial heat treatment to promote the occurrence of γ′ → γ inverse precipitation was successful.

The presence of an initial coherent γ shell appeared to enhance HeRX in LSHR, in line with the observations of Charpagne et al. on Rene´ 65 [16]. This indicates that HeRX nucleation is easier in the presence of an initial coherent γ shell, particularly in a higher misfit alloy system. This is expected as the presence of coherent γ on the rim of the primary γ′ would not only reduce the curvature of the nucleus, but also lower the interfacial energy penalty between the nucleus and the nascent HeRX γ.

However, specimens both with and without the inverse precipitation heat treatment increased in coherent boundary fraction at low levels of strain. The AR heat treatment schedule does not provide suitable conditions for inverse precipitation to occur. This suggests that inverse precipitation via a coherent gamma shell is not a prerequisite for HeRX nucleation; instead, it solely aids the HeRX mechanism. The presence of potential HeRX grains in the samples without pre-deformation heat treatment suggests that formation of a coherent γ shell produced through a specific inverse precipitation heat treatment is *unnecessary* for HeRX nucleation. This is further supported by the deviation from the classic core–shell structure. Many of the HeRX grains observed in this work form as a "lobe" on one side of a particle, rather than as a complete shell. The growth enhancement resulting from inverse precipitation is likely due to the combination of reduced curvature and a potential reduction in interfacial energy imparted by the initial coherent γ shell prior to deformation.

HeRX Nucleation in the Absence of Inverse Precipitation

In the non-HT specimens, the coherent boundary fraction substantially increases during deformation even without a heat treatment that would promote inverse precipitation. This leads us to suggest that HeRX may occur even when inverse precipitation is not active.

A different potential mechanism for nucleation off a misfitting particle can be taken from the solidification community. In recent work by O'Masta et al., molecular dynamics simulations are used to investigate the nucleation behavior of solidifying Al on a lattice-mismatched substrate. In solidification at temperatures above the melting point, a thin coherent solid layer forms on the substrate particle surface.

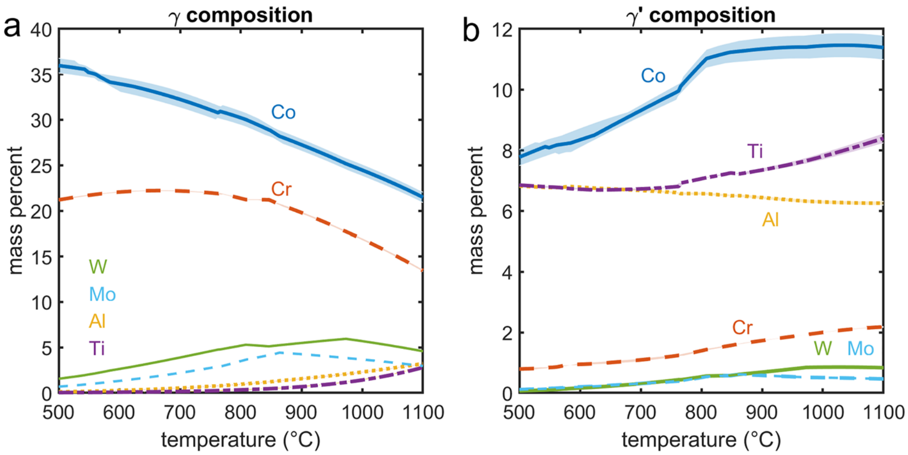

Fig. 16 Predicted composition variation in the γ (**a**) and γ′ (**b**) phases, as calculated using the Thermo-Calc software for the LSHR composition given in Table 1. Additionally, compositions calculated with ± 5% of major elements are plotted (shaded area). The γ phase is predicted to exhibit depletion in γ′ phase elements during the pre-deformation heat treatment (**a**), while the γ′ phase exhibits an enrichment in γ phase elements (**b**)

This “pseudo-morphic layer” adopts the lattice spacing of the particle. For low misfit, coherent planar growth is predicted. For medium mismatch, island growth off the pseudomorphic layer occurs, resulting in dislocations where the islands impinge. At high misfits, dislocations form directly in the pseudomorphic layer [29].

The authors suggest that a similar phenomenon with a pseudomorphic layer and potentially island growth may occur during HeRX. The “lobed” HeRX morphologies seen in this work could have arisen via island nucleation at multiple locations on the particle. However, further work on HeRX nucleation in the absence of inverse precipitation is necessary.

Lattice Misfit

In the original studies on HeRX, all alloys where the mechanism was reported had low lattice misfit [16, 18]. In contrast, the LSHR superalloy has been experimentally measured to have intermediate (0.23%) misfit at room temperature [21], which is predicted to increase at high temperatures [22]. To the authors’ knowledge this is the highest misfit alloy where HeRX has been observed to date, suggesting that the range of alloys where HeRX can be expected is broader than originally thought.

Strain Rate

When comparing the effect of strain rate on the activity of HeRX within this alloy system, the major effect is in the relative stability of the HeRX grains with increasing strain. At intermediate strains (between 0.1 and 0.3), the microstructural segmentation of the slow- and fast-forged specimens without heat treatment is nearly the same: there was a substantial increase in the fraction of suspected HeRX grains, suggesting that there is sufficient dislocation accumulation at both strain rates for HeRX to occur. Increasing prevalence of dynamic recovery in the slow-forged specimens does not appear to substantially impede HeRX activity.

At higher strains, there is a divergence in behavior between the slow- and fast-forged specimens. In the fast-forged specimens, the area fraction of potential HeRX grains decreases starting at strains of approximately 0.3, concurrent with an increase in other DDRX γ. The HeRX grains were simply able to nucleate earlier in the deformation process, but were ultimately out-competed in the overall microstructure. This is similar to the behavior observed by Charpagne et al. in their characterization of HeRX [16, 17].

In the slow-forged specimens, the observed area fraction of suspected HeRX grains (and all of the other metrics of HeRX) are remarkably stable even to high strains. This is interpreted to be the result of the interplay of HeRX with superplastic deformation. In the work of Semiatin et al., the superplastic regime for LSHR was found to occur at low strain rates ($\epsilon < 0.003$/s) and relatively high sub-solvus temperatures, though superplastic behavior was also observed at 1066 °C, which is the isothermal forging temperature used in this work [4]. Given that these conditions are very similar to those used in the processing of the slow-deformed samples, it is likely that superplastic deformation was active in these specimens. Under pure superplastic conditions, there would be negligible bulk dislocation storage and therefore no accumulated driving force for recrystallization. However, in reality, there is probably at least some conventional dislocation plasticity even under nominally superplastic deformation, resulting in a small amount of dislocation storage. Due to the low driving force necessary for HeRX, it could remain active even when other recrystallization mechanisms are suppressed. This is a potential explanation for the formation *and subsequent retention* of coherent γ in the slow-forged samples. Because no other recrystallization mechanisms are active, the HeRX grains are never consumed.

Implications of Observed HeRX Phenomenology

As this work focused on the high misfit alloy LSHR, the absence of the requirement of an initial coherent γ shell implies that the only condition necessary for the formation of HeRX grains is locally increased dislocation density around a coarse second phase particle capable of forming a coherent interface—in this system, primary γ'. Not only does this theory demonstrate why HeRX exhibits widespread activity in this system where it was not originally predicted, but it implies that HeRX activity may be achieved in all Ni-base superalloy systems to some degree.

Further, the broadened scope enabled by the absence of the preconditions on HeRX make it phenomenologically similar to PSN, perhaps on a continuum scale where the particle ranges from purely coherent to purely incoherent. However, the presence of coherency still plays an important role: it dramatically decreases the interfacial energy between the recrystallized nucleus and the particle. In the case of full coherency and low misfit, the recrystallized shell is likely to fully encircle and conform to the particle, allowing the particle to be treated as a preexisting nucleus. As misfit increases, the degree of coherency is likely to decrease, resulting in less conformation to the particle shape and perhaps a tendency toward the “lobed” morphology illustrated in Fig. 9.

For processing, the implication is that HeRX nucleation could potentially be managed by manipulating the distribution and morphology of the primary γ', similar to current practices that take advantage of incoherent particles to control PSN [30, 31]. Control over the distribution, morphology, and orientation of the primary γ' could lead to precise control of the γ recrystallized by the HeRX mechanism. In light of this and its widespread activity across a variety of forging conditions, it is reasonable to assert that control of this mechanism may provide an additional method of grain size control during forging. Accounting for the activity of this recrystallization mechanism may allow for the development of physics-based models of microstructure evolution during thermomechanical processing.

Finally, it also suggests the potential for HeRX or "HeRX-type" recrystallization mechanisms to exist in other two-phase alloy systems with a primary and secondary phase that have characteristics similar to the γ and γ' of the Ni-superalloys. As Miller et al. demonstrated that the formation of a coherent γ–γ' interface is responsible for the large reduction in the thermodynamic barrier [20], it is expected that alloys that have large particles capable of forming a coherent interface with the matrix could potentially undergo recrystallization by the HeRX mechanism. The restoration of the Burgers orientation relationship during the thermomechanical processing of two-phase Ti alloys via an analogous recrystallization mechanism was recently reported by Balachandran et al.[32] and has been exploited to control grain size during additive manufacturing [33]. Going further, Co-superalloys containing the $L1_2$ γ' phase may exhibit some type of HeRX behavior, as the matrix and γ' phase in these systems have similar crystallography to the γ and γ' phase in Ni-superalloys. If HeRX is developed into a useful mechanism for microstructural engineering, it would be possible to select a solid particle addition to control the recrystallization behavior for an arbitrary class of alloys via lattice-matching. This is the solid-state analog to the addition of a lattice-matched grain nucleant during solidification processing [34].

Conclusions

This study ultimately demonstrates that the range of conditions where HeRX can occur is broader than originally envisioned. Specifically, the following can be concluded:

- HeRX activity was observed in the LSHR superalloy, which has the highest reported misfit for an alloy demonstrating HeRX to date.
- The presence of an initial coherent γ shell formed by inverse precipitation appears unnecessary for the formation of HeRX grains. The presence of a particle capable of forming a coherent or near-coherent precipitate is sufficient. This finding implies HeRX is phenomenologically similar to PSN.
- Though not required for HeRX activity, prior heat treatment to induce inverse precipitation enhances the overall size, frequency, and area fraction of HeRX γ within the microstructure.
- At fast forging rates, HeRX nucleation is most frequent under conditions where dynamic recovery is limited. However, the HeRX grains will eventually accumulate strain during forging and be consumed by other DRX grains at higher strain levels.
- In sub-solvus heat-treated specimens, the largest HeRX grains are larger than the largest overall matrix γ grains.

Acknowledgments The authors would like to acknowledge B. Dowdell (NCSU) for the early stage SEM/EBSD data collection, and P. Fagin (AFRL and UES, Inc.) for assistance with mechanical testing and S. L. Semiatin (AFRL) for helpful discussions, as well as A. Pilchak (AFRL/RXCM), J. Shank (AFRL and UES Inc.), and J. Craggette (SOCHE and Wright State University) for assistance with DEFORM simulations and data visualizations.

Declarations

Conflict of interest The authors declare that they have no conflict of interest

References

1. R.C. Reed, *The Superalloys: Fundamentals and Applications* (Cambridge University Press, Cambridge, 2008)
2. D. Furrer, H. Fecht, JOM. **51**(1), 14–17 (1999)
3. Y. Combres, C. Levaillant, Int. J. Plast. **6**(5), 505–519 (1990)
4. S.L. Semiatin, K.E. McClary, A.D. Rollett, C.G. Roberts, E.J. Payton, F. Zhang, T.P. Gabb, Metall. Mater. Trans. A. **44A**(5), 2778–2798 (2013)
5. S.L. Semiatin, D.S. Weaver, R.C. Kramb, P.N. Fagin, M.G. Glavicic, R.L. Goetz, N.D. Frey, M.M. Antony, Metall. Mater. Trans. A. **35**(2), 679–693 (2004)
6. J.-P.A. Immarigeon, P.H. Floyd, Metall. Trans. A. **12**(7), 1177–1186 (1981)
7. A. Koul, J.-P. Immarigeon, Acta Metall. **35**(7), 1791–1805 (1987)
8. Lindsley and X. Pierron, in *Superalloys 2000 (Ninth International Symposium)*, TMS, 2000 pp. 59–68
9. P. Poelt, C. Sommitsch, S. Mitsche, M. Walter, Mater. Sci. Eng., A. **420**(1–2), 306–314 (2006)
10. B. Xie, B. Zhang, Y. Ning, M.W. Fu, J. Alloy. Compd. **786**, 636–647 (2019)
11. F.J. Humphreys, Acta Metall. **25**(11), 1323–1344 (1977)
12. F.J. Humphreys, Metal Science. **13**(3–4), 3–4 (1979)
13. F.J. Humphreys, Acta Metall. **27**(12), 1801–1814 (1979)
14. F. Li, R. Fu, F. Yin, D. Feng, H. Wang, G. Du, Y. Feng, J. Alloy. Compd. **693**, 1076–1082 (2017)
15. H.-Z. Li, L. Yang, Y. Wang, G. Tan, S.-C. Qiao, Z.-Q. Huang, M.-X. Liu, Mater. Charact. **163**, 110285 (2020)
16. M.-A. Charpagne, T. Billot, J.-M. Franchet, N. Bozzolo, J. Alloy. Compd. **688**, 685–694 (2016)
17. M.-A. Charpagne, T. Billot, J.-M. Franchet, and N. Bozzolo, in *Superalloys 2016: Proceedings of the 13th International Symposium on Superalloys*, 2016, pp. 417–426.
18. M.-A. Charpagne, P. Venne´gue`s, T. Billot, J.-M. Franchet, N. Bozzolo, J. Microsc. **263**(1), 106–112 (2016)
19. S. Katnagallu, S. Vernier, M.-A. Charpagne, B. Gault, N. Bozzolo, P. Kontis, Scripta Mater. **191**, 7–11 (2021)
20. V. Miller, E. Payton, A. Pilchak, Scripta Mater. **136**, 128–131 (2017)
21. T. Gabb: *Comparison of [gamma-gamma] prime phase coarsening responses of three powder metal disk superalloys*, NASA

technical memorandum, National Aeronautics and Space Administration, Glenn Research Center, 2016.

22. G. Olson, H.-J. Jou, J. Jung, J. Sebastian, A. Misra, I. Locci, and D. Hull, in *Superalloys 2008*, TMS (The Minerals, Metals & Materials Society), 2008 pp. 923–932.
23. S.L. Semiatin, K.E. McClary, A.D. Rollett, C.G. Roberts, E.J. Payton, F. Zhang, T.P. Gabb, Metall. Mater. Trans. A. **43**(5), 1649–1661 (2012)
24. Thermo-Calc Software AB: TCNI9/Ni-Alloys database version 9.1, 2019.
25. F. Bachmann, R. Hielscher, H. Schaeben, Solid State Phenom. **160**, 63–68 (2010)
26. S. Vernier, J.-M. Franchet, M. Lesne, T. Douillard, J. Silvent, C. Langlois, N. Bozzolo, Mater. Charact. **142**, 492–503 (2018)
27. S. Vernier, J.-M. Franchet, C. Dumont, N. Bozzolo, Metall. Mater. Trans. A. **49**(9), 4308–4323 (2018)
28. L. N. Brewer, D. P. Field, and C. C. Merriman, in *Electron Backscatter Diffraction in Materials Science*, pp. 251–262, 2009.
29. M.R. O'Masta, E.C. Clough, J.H. Martin, Comput. Mater. Sci. **192**, 110317 (2021)
30. F. Humphreys, M. Hatherly, *Recrystallization and Related Annealing Phenomena* (Pergamon, Oxford, 2004)
31. L.P. Troeger, E.A. Starke Jr., Mater. Sci. Eng. A. **293**(1), 19–29 (2000)
32. S. Balachandran, S. Kumar, D. Banerjee, Acta Mater. **131**, 423–434 (2017)
33. Z. Zou, M. Simonelli, J. Katrib, G. Dimitrakis, R. Hague, Scripta Mater. **180**, 66–70 (2020)
34. J.H. Martin, B.D. Yahata, J.M. Hundley, J.A. Mayer, T.A. Schaedler, T.M. Pollock, Nature. **549**(7672), 365–369 (2017)